International Journal of Heat and Fluid Flow 29 (2008) 967–984

Contents lists available at ScienceDirect

International Journal of Heat and Fluid Flow

journal homepage: www.elsevier.com/locate/ijhff

Active control of a free jet using a synthetic jet

David A. Tamburello [1], Michael Amitay *

Rensselaer Polytechnic Institute, Mechanical Aerospace and Nuclear Engineering, 110, 8th Street, Troy, NY 12180, USA

ARTICLE INFO

Article history:
Received 7 October 2007
Received in revised form 26 February 2008
Accepted 28 February 2008
Available online 5 May 2008

Keywords:
Synthetic jets
Active flow control
Free jet
Coherent structures

ABSTRACT

The control of an axisymmetric free jet ($Re_{U_e} = 6600$) using a single synthetic jet was investigated experimentally. The interaction was examined for a range of momentum coefficients, Strouhal numbers, and synthetic jet orientations (with respect to the main jet). To better explore the complex flow field resulting from the interaction, a rendering technique was used where three-dimensional flow fields were calculated from multiple two-dimensional measurement planes. The synthetic jet deflects the majority of the main jet flow away from it, while drawing some of the flow back toward it. Also, the synthetic jet is shown to appreciably raise the main jet's turbulent quantities, suggesting that mixing has been enhanced. Using triple decomposition, it was shown that the random and coherent motions have similar contributions to the turbulent stresses near the interaction region; whereas the coherent motions prevail farther downstream (and along the shear layers). Measurements of the streamwise vorticity showed that the interaction results in the formation of counter-rotating streamwise vortices, similar to the effect of passive tabs. The size and strength of these structures can be controlled by changing the synthetic jet's momentum coefficient, actuation frequency, or orientation. At low momentum coefficients, the largest effect is obtained for a Strouhal number of 0.32; while at higher momentum coefficients saturation is obtained due to the high excitation level. A steady control jet, which only utilizes the direct impact mechanism, results in vectoring and a deep penetration into the main jet. However, it yields decreased spreading compared to a synthetic jet with the same momentum coefficient.

1. Introduction

Over the years, free jets have become more prevalent in many industrial applications (e.g., pumps and combustors), aerospace engineering (e.g., jet engines), and more. Controlling these jets has been the focus of numerous investigations. Control techniques (passive and active) have been developed where some of the goals have been: improved mixing, noise suppression, thrust vectoring, and control of the transition from a laminar to a turbulent flow. The two dominant methods of passive flow control include noncircular nozzles (e.g., Ho and Gutmark, 1987; Gutmark and Grinstein, 1999; Zaman, 1999; and others) or the use of tabs at the nozzle exit (e.g., Bradbury and Khadem, 1975; Ahuja, 1993; Reeder and Samimy, 1996; Hileman et al., 2003; and others). While these techniques can be effective at altering free shear flows, they are mounted as permanent fixtures; thus, performance can be decreased when they are not needed or when conditions suddenly change.

Active flow control techniques include steady blowing control jets (e.g., Alvi et al., 2000; Arakeri et al., 2003; Seidel et al., 2005; Tamburello and Amitay, 2006, 2007a; and others), oscillating boundaries (e.g., Wiltse and Glezer, 1993, 1998; Pothos and Longmire, 2001), acoustic actuation (Crow and Champagne, 1971; Cohen and Wygnanski, 1987; Wicker and Eaton, 1994; Ahuja et al., 1982), or synthetic jets (e.g., Davis and Glezer, 2000; Pack and Seifert, 2001; Tamburello and Amitay, 2007b; and others).

Using flow visualization, New and Tay (2004a) showed that steady blowing control jets can weaken or even suppress the production of large-scale flow structures in the near-field region of the main jet, which suggests that the fluid injection from the control jet(s) renders the main jet shear layer unstable significantly farther upstream. Quantitative results (using PIV) were recently obtained by Tamburello and Amitay (2006) who explored the effects of the inclination angle of two steady control jets (with respect to the main jet), the main jet Reynolds number, and the velocity ratio (or momentum coefficient) of the control jets. They showed that control jets at low momentum coefficients have a stabilizing effect on the main jet while the control jets at high momentum coefficients have a destabilizing effect.

Alternatively, pulsed blowing control jets (e.g., Ibrahim et al., 2002; New and Tay, 2004b) attempt to capitalize not only on the large-scale changes via penetration but also on the actuation frequency to manipulate the large-scale, global instability modes of the base flow.

* Corresponding author. Tel.: +1 518 276 3340.
E-mail address: amitam@rpi.edu (M. Amitay).
[1] Present address: Savannah River National Laboratory, Savannah River Site, Aiken, SC 29808, USA.

0142-727X/$ - see front matter © 2008 Elsevier Inc. All rights reserved.
doi:10.1016/j.ijheatfluidflow.2008.02.017

Nomenclature

C_μ	momentum coefficient, $C_\mu = \frac{n\bar{I}_j}{\frac{1}{2}\rho U_e^2 d_e^2}$
d_e	main jet exit diameter
d_{si}	synthetic jet orifice diameter
f	actuation frequency
$\bar{I}_j$	time-averaged synthetic jet momentum during the outstroke, $\bar{I}_j = \frac{1}{\tau}\rho d_{sj}^2 \int_0^\tau u_j^2(t)dt$
n	number of active synthetic jets ($n = 1$ in the present paper)
Re_{U_e}	main jet Reynolds number, $\mathrm{Re}_{U_e} = \frac{U_e d_e}{\nu}$
St_r	Strouhal number, $St_r = \frac{fd_e}{U_e}$
T	actuation period time, $T = \frac{1}{f}$
t	time
U	streamwise velocity component
$u_j(t)$	phase-averaged velocity at the synthetic jet exit plane
U_{cl}	streamwise centerline velocity of the main jet
U_e	main jet exit velocity
U_j	synthetic jet peak velocity
U_{max}	maximum streamwise velocity of the main jet
U_0	streamwise centerline velocity at $x/d_e = 0.5$
$\bar{U}_{pa}$	streamwise phase-averaged velocity
$\bar{U}_{ta}$	streamwise time-averaged velocity
$\tilde{u}'^2$	total streamwise normal stress
$u_c'^2$	coherent streamwise normal stress
$u_r'^2$	random streamwise normal stress
$\tilde{u}'\tilde{v}'$	total shear stresses in x–y plane
$u_c'v_c'$	coherent shear stresses in x–y plane
$u_r'v_r'$	random shear stresses in x–y plane
$\tilde{u}'\tilde{w}'$	total shear stresses in x–z plane
$u_c'w_c'$	coherent shear stresses in x–z plane
$u_r'w_r'$	random shear stresses in x–z plane
V	cross-stream velocity component
V_{total}	total velocity; $V_{total} = \sqrt{U^2 + V^2 + W^2}$
$\tilde{v}'^2$	total cross-stream normal stress
$v_c'^2$	coherent cross-stream normal stress
$v_r'^2$	random cross-stream normal stress
W	spanwise velocity component
$\tilde{w}'^2$	total spanwise normal stress
$w_c'^2$	coherent spanwise normal stress
$w_r'^2$	random spanwise normal stress
x	streamwise direction
y	cross-stream direction
z	spanwise direction

Greek symbols

α	angle of the synthetic jet centerline with respect to the main jet centerline
δ	jet width in the x–y plane defined at the cross-stream locations where $U = U_{max}/2$
δ_z	jet width in the x–z plane defined at the spanwise locations where $U = U_{max}/2$
φ	phase along the synthetic jet cycle
ν	kinematic viscosity
$\widehat{\Omega}_x$	normalized streamwise vorticity, $\widehat{\Omega}_x = (\frac{\partial W}{\partial y} - \frac{\partial V}{\partial z})\frac{d_e}{U_e}$
$\widehat{\Omega}_y$	normalized cross-stream vorticity, $\widehat{\Omega}_y = (\frac{\partial U}{\partial z} - \frac{\partial W}{\partial x})\frac{d_e}{U_e}$
$\widehat{\Omega}_z$	normalized spanwise vorticity, $\widehat{\Omega}_z = (\frac{\partial V}{\partial x} - \frac{\partial U}{\partial y})\frac{d_e}{U_e}$
ρ	air density
τ	synthetic jet outstroke time, $\tau = T/2$

Earlier investigations chose to employ purely time-periodic flow control methods, such as the introduction of global axisymmetric acoustic excitation, rather than using the direct impact techniques described above. Acoustic excitation, such as using a speaker in the plenum (e.g., Crow and Champagne, 1971) or an azimuthal array of speakers (e.g., Cohen and Wygnanski, 1987; Petersen and Samet, 1988), has been shown to amplify the axisymmetric mode ($m = 0$) in order to manipulate large-scale, global instabilities in the base flow.

Another form of time-periodic active flow control, which is the main focus of this paper, is the use of synthetic jet actuators. Synthetic jet actuators capitalize on the direct impact (similar to steady blowing control jets) as well as the manipulation of large-scale, flow instabilities within the main jet through their near-field periodic motion. A review of this technology, including a description of the synthetic jet and its application, is provided in the review by Glezer and Amitay (2002). Unlike other fluidic control methods, synthetic jet actuators are synthesized from the working fluid of the flow system and, thus, can transfer momentum to the flow without net mass injection across the flow boundary while eliminating the need for an additional fluid source and extraneous pumping and piping (e.g., Smith and Glezer, 1998, 2002; Cannelle and Amitay, 2005; Amitay and Cannelle, 2006). Davis and Glezer (2000) used nine synthetic jets (around the circumference of the main jet) to control the main jet and to enhance mixing. Davis (2000) used pulse modulation of synthetic jet actuators placed at the orifice of an axisymmetric jet nozzle to control mixing by concurrently manipulating both the small- and large-scale dynamical processes. Pack and Seifert (2001) showed that synthetic jets with high-amplitude excitation at the main jet exit cause vectoring and enhanced spreading rates on the excited side.

Clearly, a lot of work has been conducted on the control of a free jet. However, there is still a lack of understanding of the complex three-dimensional interaction of a *single* synthetic jet with an axisymmetric free jet. Therefore, the motivation of the present paper is to explore the three-dimensional interaction of an axisymmetric free jet with a single synthetic jet through a parametric study. The parameters studied were: the momentum coefficient, the driving frequency, and the angle of the synthetic jet (with respect to the centerline of the main jet).

2. Experimental setup and procedure

The experiments were conducted in a 1.56 m × 0.72 m × 0.72 m clear-walled enclosure, using the same jet assembly as the previous work of Tamburello and Amitay (2006, 2007a). The jet assembly consists of four components: an inlet section, a seeding chamber, a swirl chamber, and a converging nozzle (Fig. 1a). In the present experiment, the seeding and swirl chambers were not activated, and their openings were sealed. Each of the four assembly components is made from stainless steel and is coated with an anti-abrasive Nickel Silicon Carbide layer, with an approximate thickness of 13 μm, to prevent erosion over time. The converging nozzle (having a fifth-order spline curvature and an area ratio of 10:1) has an exit diameter, d_e, of 4 mm and attachment points for the flow control modules. This assembly yields a uniform velocity for ~80% of the orifice diameter with a 0.1% turbulence level at the jet exit plane.

As was mentioned above, the control of the free jet is performed using a single synthetic (zero-net-mass-flux) jet that is issued at an angle of $\alpha = 30°$ or 60° with respect to the free jet (Fig. 1a). These angles were chosen as representative cases to ensure that the interaction between the synthetic jet and the free jet occurs within the free jet's developing region. To create the synthetic jet actuators, a specially designed control module (made with stereolithography) was attached directly to the jet assembly, as shown in

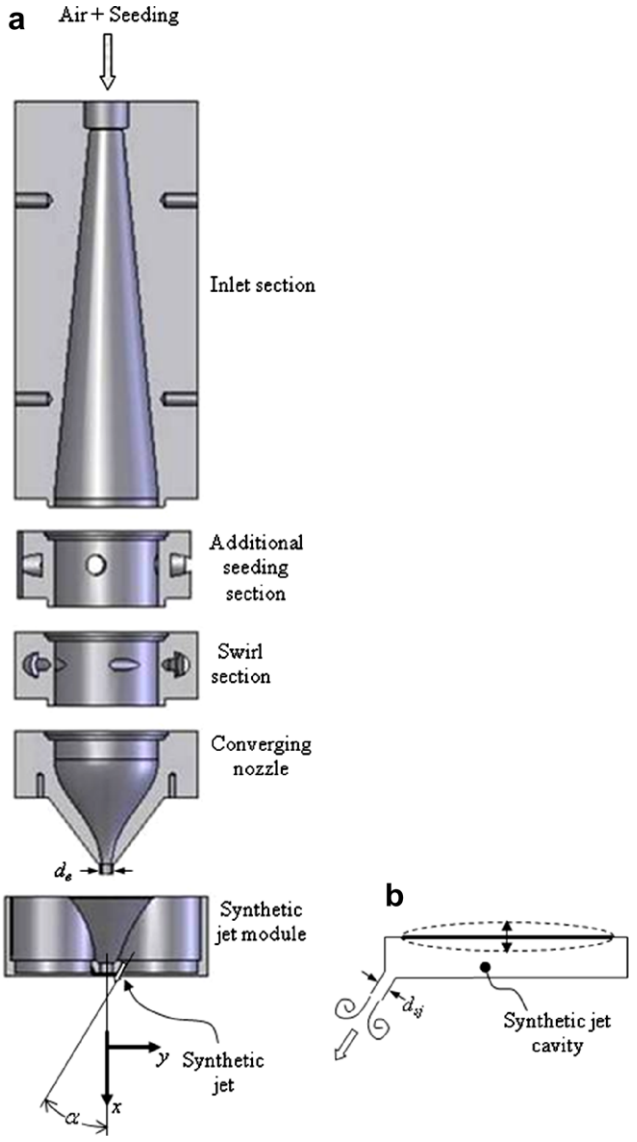

Fig. 1. Schematic of the jet assembly (a) and the synthetic jet actuator (b).

Fig. 1a, such that the synthetic jet edge is approximately $d_e/2$ from the edge of the main jet orifice. The synthetic jet is issued through a 1.2 mm circular orifice as a result of the periodic motion of a piezoelectric disk that is mounted on one of the walls of a sealed cavity, as illustrated in Fig. 1b. Note that Fig. 1a presents the exploded view to better visualize each component. Here, the main jet Reynolds number (Re_{U_e}) is held fixed at 6600 (based on the main jet exit velocity of 25 m/s and an orifice diameter of 4 mm). The driving frequency of the synthetic jet ranges from 1000 Hz to 3000 Hz (with a corresponding Strouhal number, St_r, of 0.16–0.48). The strength of the synthetic jet relative to the main jet is quantified using the momentum coefficient, C_μ (in the present experiments, $0.005 < C_\mu < 0.16$, with a corresponding synthetic jet to main jet velocity ratio of $0.35 < U_j/U_e < 2.88$). The maximum synthetic jet velocity is 72 m/s.

In the current study, a LaVision particle image velocimetry (PIV) system was used, where the velocity vectors were calculated using a cross-correlation technique with adaptive multi-pass, deformable interrogation windows (single pass at 64 × 64 and two passes at 32 × 32 pixels) with 50% overlap. The camera was mounted at a perpendicular distance of ~0.4 m to the laser light sheet such that the distance between pixels is 27.8 μm. The maximum main jet velocity (25 m/s) corresponds to an average displacement of approximately 10.5 pixels with an error of approximately ±0.1 pixel (±0.5 m/s).

Ensemble averages and turbulent quantities were calculated from a sequence of 500 image pairs, where the accuracy was deemed sufficient since the primary focus is flow field comparison with and without flow control. The instantaneous velocity vectors were validated using the RMS of their eight neighboring vectors, where any vector that was greater than 250% of the RMS was replaced by the average of the neighboring vectors. In addition, the time-averaged and turbulent quantities were smoothed using the eight neighboring vectors with 50% of the final value being calculated from the eight neighboring vectors.

A LabView code was written to synchronize the LaVision PIV system's programmable timing unit with the actuation cycle of the synthetic jet to capture phase-locked data. Using this code two signals were generated, one that served as the driving signal for the synthetic jet and another that served as the trigger for the PIV data acquisition system, which was a TTL signal at a submultiple of the synthetic jet's driving signal. The acquisition system was then locked at a specific phase by changing the time delay between these two signals. In this manner, data are only acquired at a given phase along the synthetic jet cycle for all 500 image pairs.

Throughout the experiments, the synthetic jet was always oriented along the x–y plane, where the orientation of the camera and the dual-pulse laser varied for measurements along (x–y plane) or across (x–z plane) the synthetic jet's plane. To better understand the complex flow field resulting from the interaction of a single synthetic jet with the main jet, data were acquired at five x–z planes and seven x–y planes. In addition, a data reduction technique (similar to the technique developed by Schabacker and Bölcs, 1996 and Sakakibara et al., 2001) was used to create three-dimensional flow renderings. In order to improve the spatial resolution, the 35 measurement points (marked with closed symbols in Fig. 2) were expanded to 117 points at each streamwise location via linear and bi-linear interpolations (marked with open symbols in Fig. 2) of the measured, two-dimensional data points. This grid

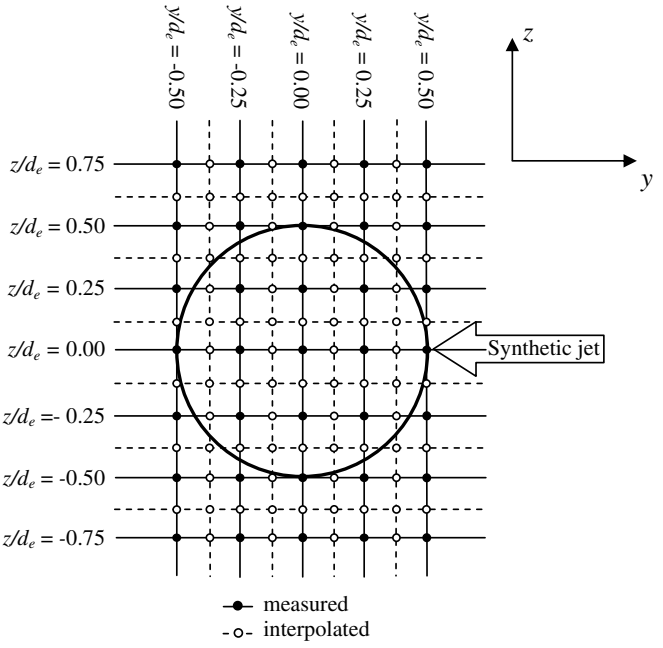

Fig. 2. Grid used to generate the 3D flow fields (main jet direction is off of the plane).

does not capture structures smaller than 1 mm; however, it captures the large vortical structures and provides valuable insight on the global interactions between the synthetic jet and the main jet. The smaller size structures were explored by analyzing the data at the measured, individual two-dimensional planes that had higher spatial resolution.

3. Results

The interaction of an axisymmetric free jet with a single synthetic jet actuator is presented in this section. First, the effect of the synthetic jet on the time- and phase-averaged flow fields and on the turbulence quantities of the main jet, at fixed synthetic jet angle and Strouhal number, with varying momentum coefficient, is presented in Section 3.1. Section 3.2 presents the effect of the synthetic jet angle, while a comparison between steady control and synthetic jets is discussed in Section 3.3. Section 3.4 presents the effects of the Strouhal number.

3.1. Interaction of the main jet with a synthetic jet at $\alpha = 30°$

The interaction of a single synthetic jet at $\alpha = 30°$ with the free jet is presented in this section. The normalized mean spanwise and cross-stream vorticity fields ($\widehat{\Omega}_z$ and $\widehat{\Omega}_y$, respectively) were calculated from the velocity vector fields (not shown) and are presented in Fig. 3 for the x–y and x–z centerline measurement planes (Fig. 3a–d and e–h; $z/d_e = 0$ and $y/d_e = 0$, respectively). As expected, the vorticity of the baseline jet (Fig. 3a and e) is concentrated in radial locations corresponding to the jet's shear layer with positive vorticity along the left-side shear layer and negative vorticity (represented by the dashed lines) along the right-side shear layer. In the potential core ($x/d_e < 5$), the width of the vorticity layer remains relatively constant (with the highest vorticity concentrations) while, farther downstream, where instabilities grow, the vorticity magnitude decreases as the jet widens. Instantaneous vorticity distributions (not shown here; however, are included in our previous work, Tamburello and Amitay, 2007b) confirm the formation and evolution of vortex rings, as was described by Yule (1978).

When the synthetic jet is activated with $C_\mu = 0.01$ (Fig. 3b), the cross-stream extent of the normalized vorticity increases while the vorticity disperses closer (than the baseline case) to the main jet exit. Farther downstream, the synthetic jet impinges on the main jet resulting in an asymmetric vorticity distribution with a rapid decrease in its magnitude along the right side (closer to synthetic jet) and increased spreading in both directions. Along the left-side shear layer, the vorticity distribution remains relatively constant for $x/d_e < 1.5$, followed by a rapid increase in width and decreased magnitude. Similar trends were also seen at $z/d_e = 0.25$ and 0.5 (off centerline, not shown) where the effect of the synthetic jet is felt throughout the entire main jet flow field. The effects of the synthetic jet on the main jet are attributed to two mechanisms: (1) the excitation and amplification of the main jet natural modes, and (2) the direct impact of the synthetic jet into the main jet. These mechanisms will be discussed in detail later.

As the momentum coefficient is increased to 0.04 and 0.08 (Fig. 3c and d, respectively), the cross-stream width of the normalized vorticity increases further while its magnitude begins to decrease closer to the main jet exit.

Along the x–z centerline measurement plane (Fig. 3f–h), the impact of the synthetic jet onto the main jet is clearly visible as shown by the dashed line marking the streamwise interaction locations at $x/d_e \approx 1.8$, 1.7, and 1.6 for $C_\mu = 0.01$, 0.04, and 0.08, respectively. At these locations, the vorticity distributions widen abruptly due to the penetration of the synthetic jet as well as the wrapping of the main jet around the impulse. Note the presence of a counter-rotating vortex pair at $x/d_e = 1.8$ (Fig. 3g and h) corresponding to the synthetic jet impact.

To explore the effects of the momentum coefficient on the three-dimensional interaction between a synthetic jet and the main jet, a rendering technique was implemented for the baseline and phase-averaged velocity fields (at $\phi = 240°$) and is presented in Fig. 4. These renderings are represented by three iso-velocity surfaces, corresponding to $V_{total}/U_e = 0.65$, 0.7, and 0.75. Due to the relatively coarse nature of the grid, some smaller structures do not appear in these three-dimensional renderings. However, these renderings successfully show the global fluid motions and therein lies their benefit.

The baseline jet flow field (Fig. 4a) is axisymmetric about the jet's centerline. At a momentum coefficient of 0.01 (Fig. 4b), the impulse from the synthetic jet's previous actuation cycle penetrates through the main jet (at this total velocity level) while the current impulse creates an indention on the synthetic jet side of the main jet flow (at $x/d_e = 1.2$). This indentation becomes larger with increasing momentum coefficient ($C_\mu = 0.04$ and 0.08, Fig. 4c and d, respectively). In addition, the main jet widens with increasing momentum coefficient and a portion of the iso-surface stretches outside of the measurement grid as can be seen by the discontinuity in the renderings.

While the three-dimensional renderings show the global behavior, the corresponding two-dimensional, phase-locked vorticity distributions (Fig. 5) show the small-scale structures necessary to better understand the effects of the momentum coefficient, where Fig. 5a–c and d–f correspond to data taken in the x–y and x–z centerline planes, respectively, at a phase of 240°. At a momentum coefficient of 0.01 (Fig. 5a and d), the effect of the synthetic jet is both to increase the size of the main jet's vortex rings as well as penetrate through the main jet's shear layer, which disrupts its development. Note the two pairs of counter-rotating vortices (marked by dashed circles in Fig. 5d), which correspond to the synthetic jet's two consecutive cycles.

As the momentum coefficient is increased ($C_\mu = 0.04$ and 0.08, Fig. 5b–c and e–f for the x–y and x–z planes, respectively), the synthetic jet's impulse penetrates deeper into the main jet flow, which further alters the main jet's downstream development. In addition, the vorticity associated with the synthetic jet's vortex ring emerges into the x–z measurement plane, as marked by the arrows in Fig. 5e and f. Note that the vorticity distribution is wider with increasing momentum coefficient in both the x–y and x–z measurement planes.

The penetration of the synthetic jet into the main jet, as shown by the indentation in the three-dimensional phase-averaged renderings (Fig. 4), results in a bending and tilting of its vortical structures and the formation of streamwise vortices. To show these structures, the normalized streamwise vorticity, $\widehat{\Omega}_x$, was calculated and is presented in multiple y–z planes for the time-averaged forced cases with $C_\mu = 0.01$, 0.04, and 0.08 (Fig. 6a–c, respectively). When the synthetic jet is activated at $C_\mu = 0.01$ (Fig. 6a), it penetrates into the main jet where the geometric intersection location between the main jet centerline and the synthetic jet centerline is at $x/d_e = 1.5$ (near the second y–z plane from the orifice in Fig. 6a). The impact of the synthetic jet can be clearly seen by the counter-rotating vortices (marked by the bold dashed circles) at $x/d_e = 1.42$. Moreover, the synthetic jet bends the main jet vortex rings away from the synthetic jet and tilts them in the streamwise direction, resulting in a pair of streamwise rollers with opposite sense that are wrapped around the synthetic jet's impulse. At $x/d_e = 2.59$ (third y–z plane from the orifice in Fig. 6a), the vorticity associated with the synthetic jet is significantly diminished and is wrapped by the main jet. Farther downstream, the synthetic jet's impulse is completely dispersed and the streamwise vorticity fields in the y–z planes consist of a pair of counter-rotating vortices

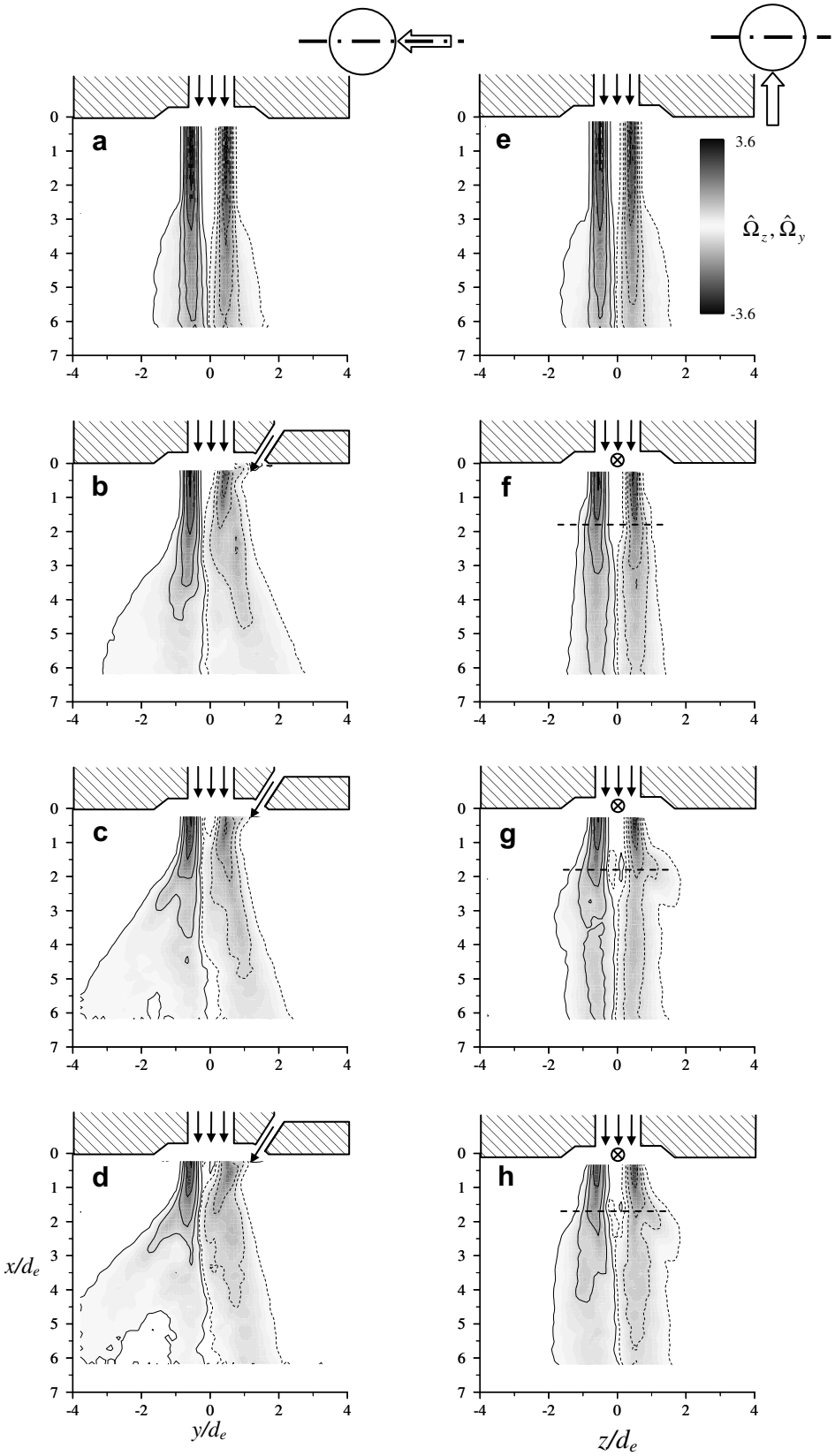

Fig. 3. Mean vorticity fields of the baseline jet (a, e) and the forced jets with $C_\mu = 0.01$ (b, f), 0.04 (c, g), and 0.08 (d, h) in the x–y (a–d) and x–z (e–h) centerline measurement planes.

above and below $z/d_e = 0$, which are due to the bending and tilting of the main jet.

Note that Zaman et al. (1994) showed a similar pair of counter-rotating vortices in their streamwise vorticity measurements on a

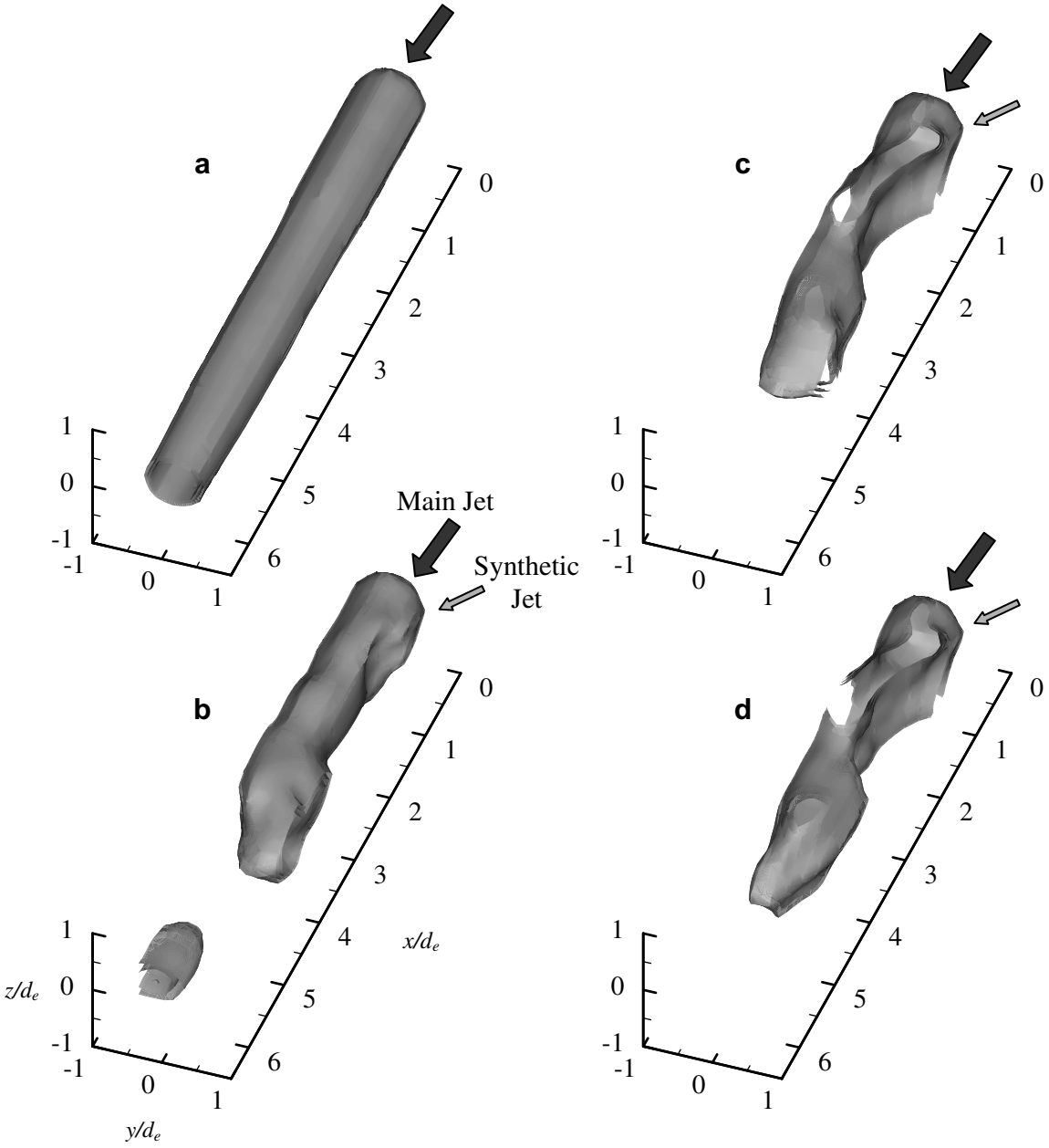

Fig. 4. Three-dimensional iso-total velocity surfaces of the baseline (a) and phase-averaged forced jet at $\phi = 240°$ for $C_\mu = 0.01$ (b), 0.04 (c), and 0.08 (d). $V_{total}/U_e = 0.65$, 0.7, and 0.75.

Mach 0.3 jet that was instrumented with a single delta tab mounted at its orifice. In a later paper Zaman (1999) showed similar vorticity structures for asymmetric nozzles as well as tabbed nozzles at multiple Mach numbers. Both Zaman et al. (1994) and Zaman (1999) provided sketches of the likely vorticity distribution within their main jet flow field, which are similar to the vorticity distribution shown in the y–z plane at $x/d_e = 1.42$ (second y–z plane from the orifice in Fig. 6a). In addition, Tamburello and Amitay (2007c) showed a three-dimensional schematic representation of the vortex interaction.

As the synthetic jet's momentum coefficient is increased to 0.04 and 0.08 (Fig. 6b and c, respectively), it penetrates the main jet much deeper and its presence is much more pronounced both in the magnitude of the streamwise vortical structures of the synthetic jet's impulse as well as in the main jet's pair of streamwise counter-rotating structures that wrap around the synthetic jet. Near the intersection location for $C_\mu = 0.08$ (second y–z plane from the orifice in Fig. 6c), the effect of the synthetic jet is felt throughout the entire plane. Farther downstream, the streamwise vorticity fields exhibit two large counter-rotating vortices of the warped shear layer vorticity where the presence of the synthetic jet diminishes by $x/d_e = 4.93$ (fifth y–z plane from the orifice in Fig. 6c).

Next, the effect of the synthetic jet on the main jet turbulence field was investigated by calculating the turbulent stresses with and without the activation of the synthetic jet. Distributions of the turbulent stresses of the baseline jet (without the introduction of the synthetic jet) are presented in Fig. 7, where the normalized streamwise normal stress, cross-stream normal stress, and the shear stress are shown in Fig. 7a–c, respectively. The streamwise normal stress distribution ($\overline{u'^2}/U_e^2$,Fig. 7a) is symmetric about the x-axis, with near-zero values in the potential core and highest values along the shear layers (i.e., double-peak distribution). Fig. 7b

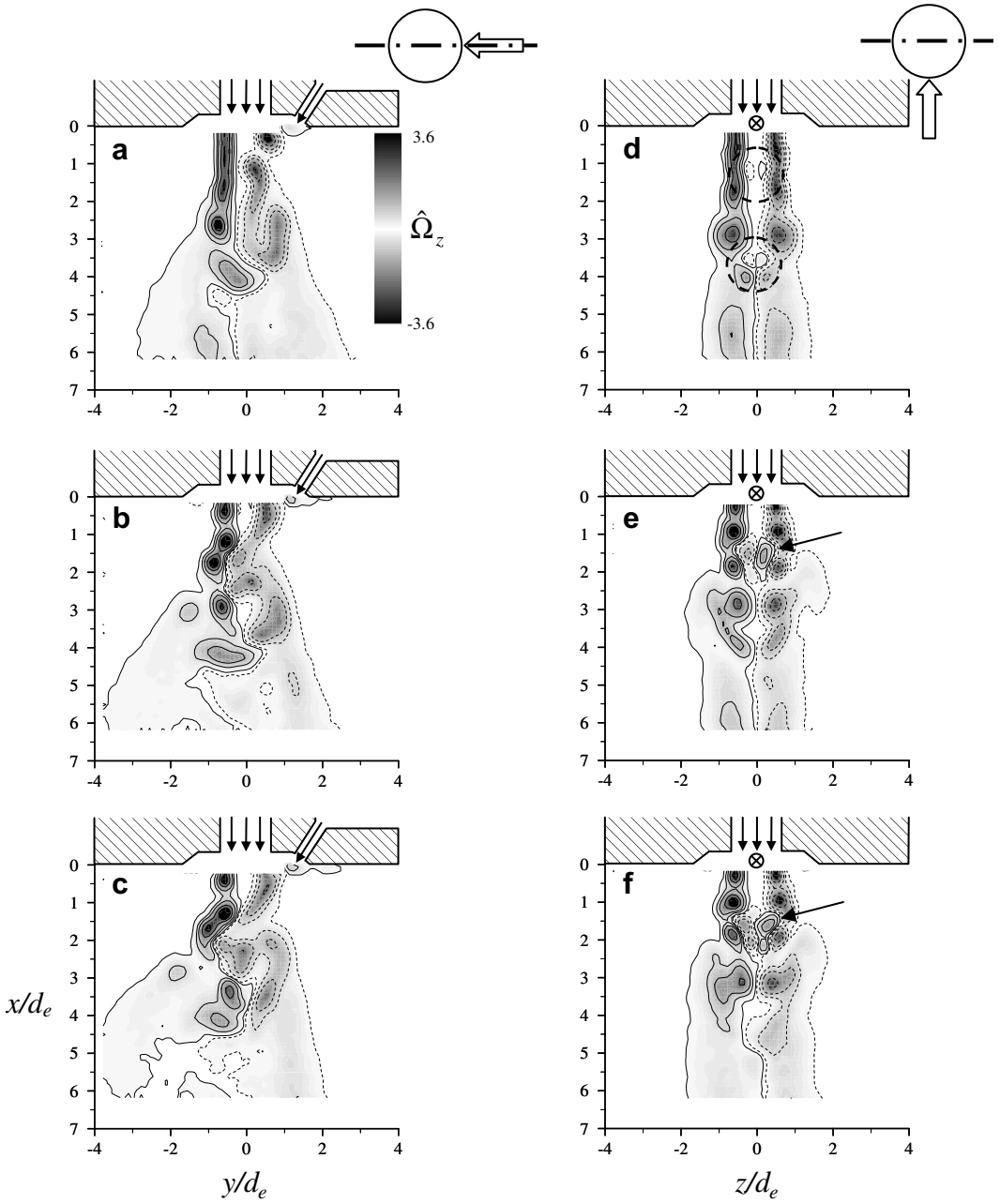

Fig. 5. Phase-averaged vorticity fields at $\varphi = 240°$ for $C_\mu = 0.01$ (a, d), 0.04 (b, e), and 0.08 (c, f) in the x–y (a–c) and x–z (d–f) centerline planes.

shows the distribution of the normalized cross-stream normal stress, $\tilde{v}'^2/U_e^2$, which is also symmetric about the x-axis, with near-zero values for $x/d_e < 2$. Farther downstream, $\tilde{v}'^2/U_e^2$ has a similar distribution to $\tilde{u}'^2/U_e^2$; however, the magnitudes are lower throughout the measurement domain. The distribution of the normalized shear stress, $\tilde{u}'\tilde{v}'/U_e^2$ (Fig. 7c), is anti-symmetric about the x-axis and is concentrated in the shear layers of the jet, with positive values along the right-side shear layer and negative values (marked by dashed contour lines) along the left-side shear layer, due to the opposite velocity gradients in the shear layers. The shear stress is very small in the potential core and in a narrow region along the jet centerline where the velocity gradients are approximately zero. These distributions are similar to those observed by Yule (1978) and Alkislar et al. (2005).

The effect of the synthetic jet on the turbulence field can be best appreciated by decomposing each component of the turbulent quantities into its coherent and random components using the triple decomposition technique (see Tamburello and Amitay, 2007b, for analysis explanation). In order to conduct the triple decomposition, both time-averaged and phase-averaged (to the actuation waveform) data were acquired.

Fig. 8 presents the normalized streamwise, cross-stream, and shear stresses where the total turbulent stresses are shown in Fig. 8a, d and g; the coherent stresses are presented in Fig. 8b, e and h; while Fig. 8c, f and i corresponds to the random turbulent stresses. Here, $C_\mu = 0.01$ and the data were acquired in the x–y centerline ($z/d_e = 0$) plane (similar effects were also obtained for other momentum coefficients). When the synthetic jet is activated, the streamwise normal stresses increase at the shear layers along the synthetic jet's line of action with maximum values at $x/d_e \approx 1.2$, $y/d_e \approx 0.4$ and $x/d_e \approx 3.2$, $y/d_e \approx -0.7$. The significant increase in $\tilde{u}'^2/U_e^2$ is due to the penetration of the synthetic jet into the main

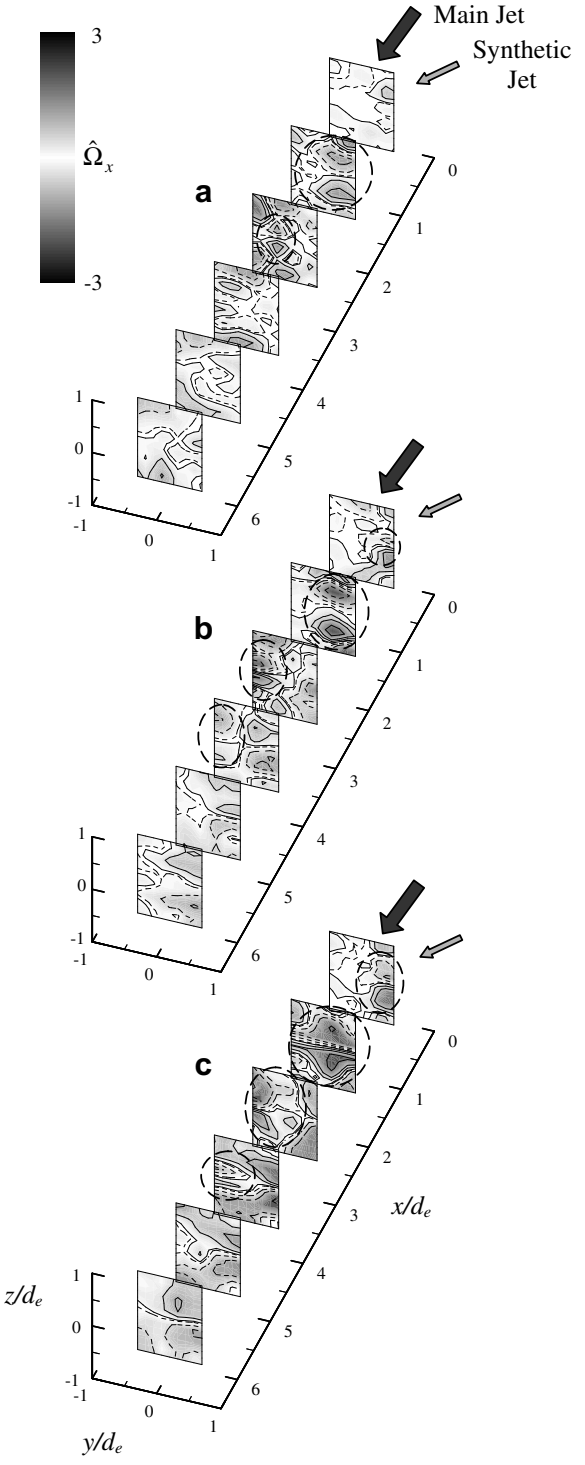

Fig. 6. Streamwise vorticity of the forced jet with C_μ = 0.01 (a), 0.04 (b), and 0.08 (c). y–z planes from x/d_e = 0.25–6.10 with a spacing of $\Delta x/d_e$ = 1.17.

jet, thus disrupting the main jet shear layer around these locations. Therefore, near the intersection location, the synthetic jet yields large random stresses (Fig. 8c) while the coherent fluctuations (Fig. 8b) have the largest contribution to the total streamwise stresses farther downstream.

The cross-stream normal stresses for the forced case are shown in Fig. 8d–f. The total turbulent stress (Fig. 8d) exhibits a non-symmetric distribution where the highest magnitude is at $x/d_e \approx 3.2$ and $y/d_e \approx -0.4$, corresponding to the interaction location of the synthetic jet with the main jet on the side opposite the synthetic

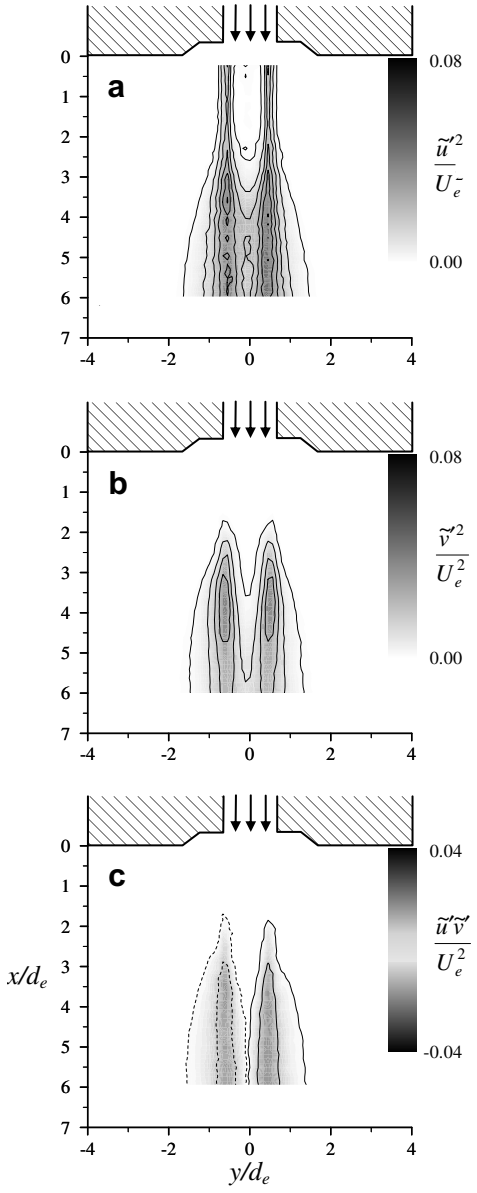

Fig. 7. Distributions of normalized streamwise (a) and cross-stream (b) normal stresses and shear stress (c) for the baseline jet.

jet. At this location, the total cross-stream stresses are comprised of both the coherent and random motions (Fig. 8e and f, respectively). Farther downstream, the random fluctuations diminish and the total stresses are governed by coherent motions.

The distributions of the total, coherent, and random turbulent shear stresses are presented in Fig. 8g–i, respectively. The normalized total turbulent shear stress (Fig. 8g) exhibits a higher concentration along the shear layer on the side closer to the synthetic jet. The contribution of the coherent shear stress to the total shear stress is very small throughout the measurement domain (Fig. 8h), while the random shear stress (Fig. 8i) has a much larger contribution, especially near the interaction region ($1 < x/d_e < 4.5$). The coherent motions are due to the periodic nature of the synthetic jet, which amplifies the large vortical structures, resulting in a wider jet and, thus, smaller velocity gradients and smaller coherent shear stresses.

The effect of the synthetic jet on the turbulent stresses in the x–z centerline ($y/d_e = 0$) plane is presented in Fig. 9. The total turbulent stresses are presented in Fig. 9a, d and g; the coherent stres-

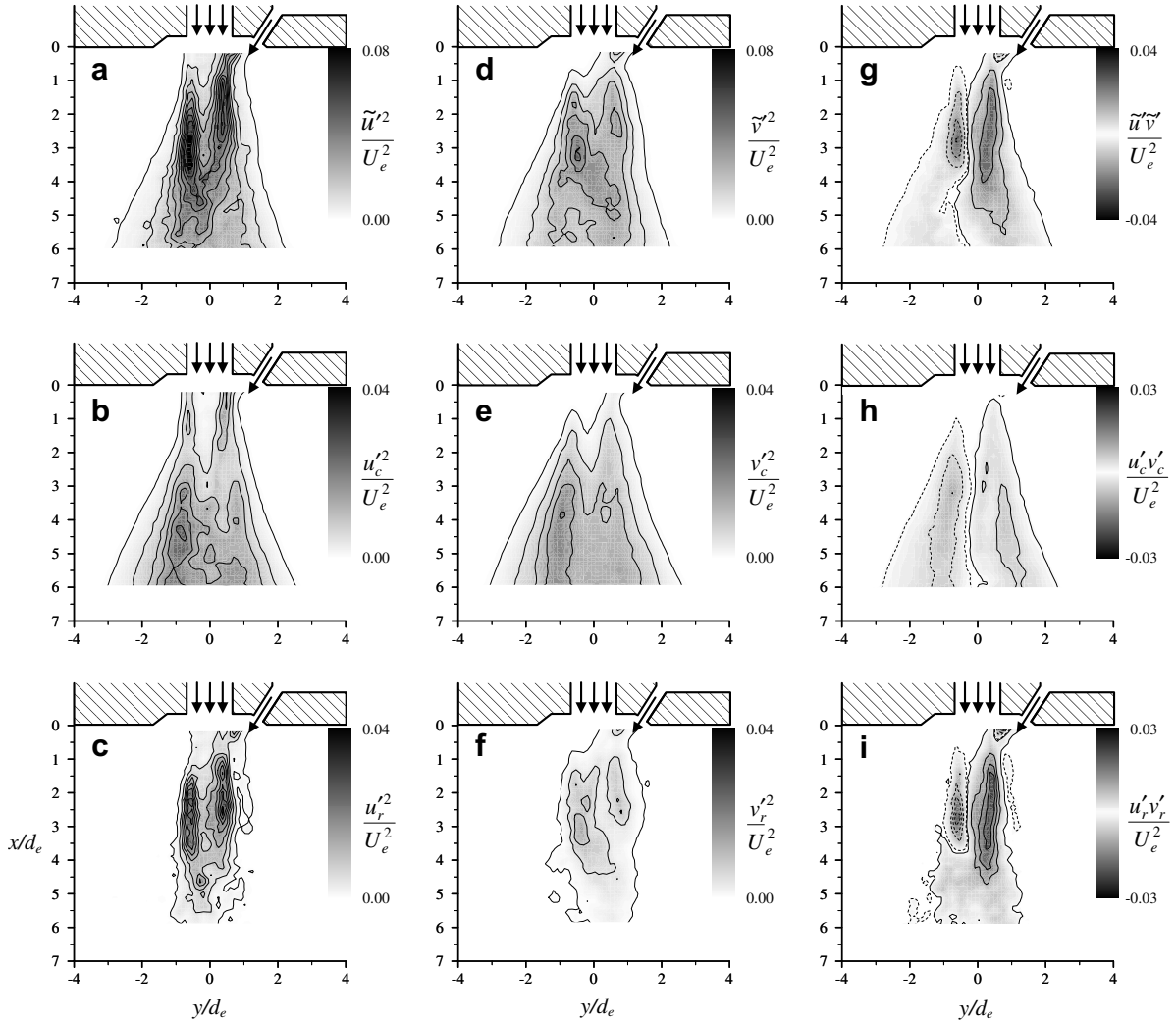

Fig. 8. Contours of the turbulent stresses: streamwise normal component (a–c), cross-stream normal component (d–f), and shear stresses (g–i). Total stresses (a, d, g), coherent stresses (b, e, h), and random stresses (c, f, i). x–y centerline plane. $C_\mu = 0.01$.

ses are shown in Fig. 9b, e and h; while the random turbulent stresses are presented in Fig. 9c, f and i. All three total turbulent stresses (Fig. 9a, d and g) exhibit symmetric distributions (about the x-axis) with higher values compared to the corresponding baseline stresses (Fig. 7a–c, respectively). As in the x–y plane, the contribution of the coherent motions to the normal streamwise and cross-stream stresses (Fig. 9b and e, respectively) is larger (than the random fluctuations, Fig. 9c and f, respectively). However, the contribution of the coherent and random shear stresses (Fig. 9h and i, respectively) to the total shear stress is similar, where the random stresses have slightly higher magnitudes near the interaction domain and the coherent stresses have higher magnitudes farther downstream.

The data presented in Figs. 7–9 show that the interaction of the free jet with a synthetic jet results in a significant increase in the normal and shear stresses. Near the interaction location, the contribution of the random motion is slightly larger due to the direct impact of the synthetic jet onto the main jet, while farther downstream the flow is dominated by coherent motions due to the amplification of the naturally unstable modes of the free jet.

3.2. Effect of the synthetic jet orientation

Previous work by Tamburello and Amitay (2007b) discussed the three-dimensional interaction of the main jet with the synthetic jet that was oriented perpendicular to the free jet. The main objective was to investigate the effect of the upstream location of the synthetic jet (i.e., inside the nozzle of the main jet). They showed that the interaction is affected by the same two mechanisms (i.e., (1) direct impact of the synthetic jet into the main jet, and (2) amplification of unstable modes of the main jet). Furthermore, increasing the distance between the synthetic jet exit and the main jet nozzle exit decreased the effectiveness of the synthetic jet's impulse, resulting in smaller jet vectoring, weaker streamwise vortical structures, and decreased turbulence levels.

In the present paper, the interaction between the main jet and the synthetic jet occurs outside the main jet orifice, and the effect of the synthetic jet orientation is investigated. This enables further exploration of the interaction mechanisms associated with the activation of the synthetic jet. Fig. 10 presents the velocity vector fields for the baseline (Fig. 10a) and forced jet cases with $\alpha = 30°$ (Fig. 10b–d) and 60° (Fig. 10e–g) for $C_\mu = 0.01$ (Fig. 10b and e), 0.04 (Fig. 10c and f), and 0.08 (Fig. 10d and g) along the x–y centerline plane. The corresponding velocity vector fields along the x–z centerline plane are presented in Fig. 11. Note that the arrow (and the number "1.0") shown in Fig. 10a represents a normalized velocity of unity. As expected, the baseline jet (Fig. 10a) is symmetric about the x-axis and its potential core extends to $x/d_e \approx 5$. In addition, the velocity profile near the orifice is uniform for ~80% of the orifice diameter.

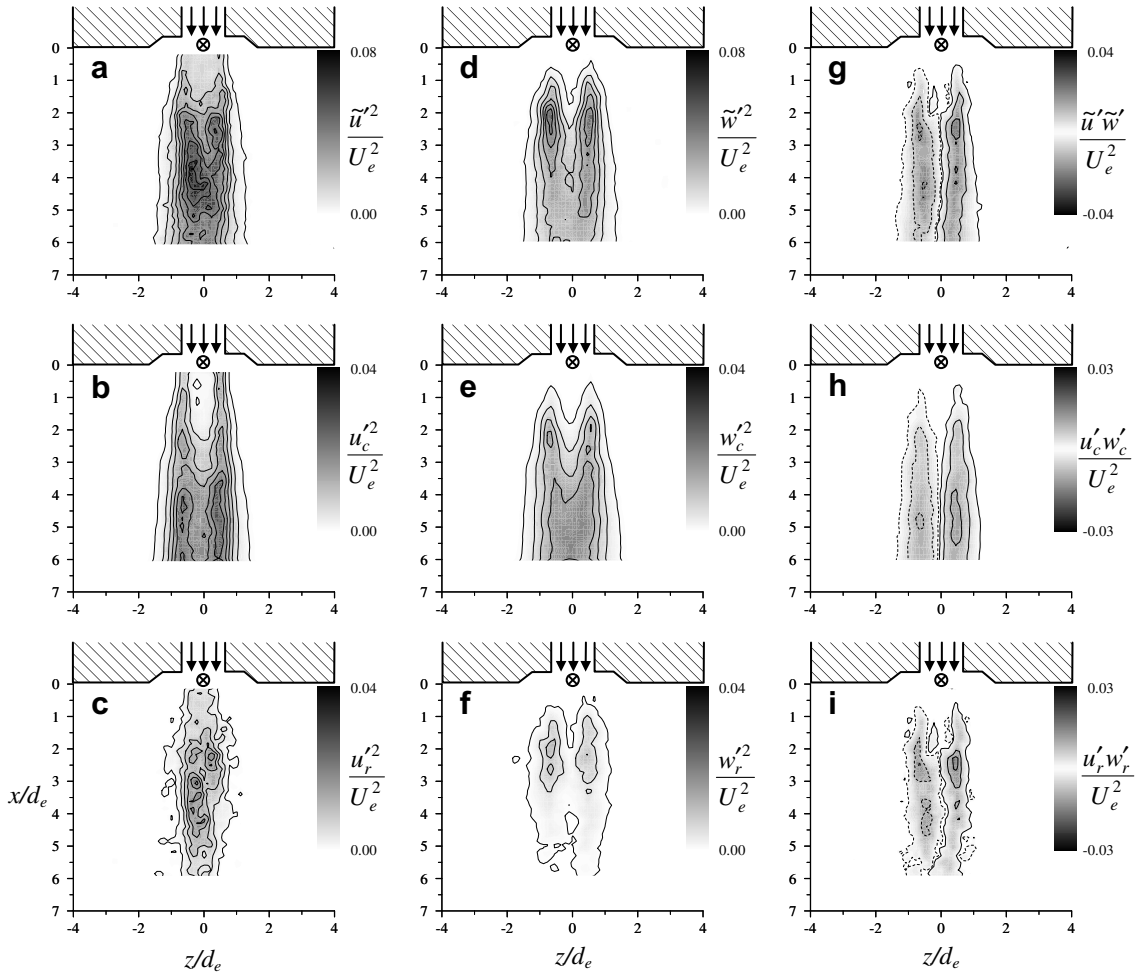

Fig. 9. Contours of the turbulent stresses: streamwise normal component (a–c), cross-stream normal component (d–f), and shear stresses (g–i). Total stresses (a, d, g), coherent stresses (b, e, h), and random stresses (c, f, i). x–z centerline plane. $C_\mu = 0.01$.

When the synthetic jet is activated at $\alpha = 30°$ with the low momentum coefficient ($C_\mu = 0.01$, Fig. 10b), the streamwise extent of the potential core is reduced, the main jet's width is increased, and the main jet flow is tilted away from the synthetic jet (the dashed line marks the trajectory of the maximum velocity). As mentioned previously, these effects can be attributed to two mechanisms: (1) direct impact of the synthetic jet onto the main jet, and (2) the growth of the vortical coherent structures due to the synthetic jet's frequency. As the momentum coefficient is increased to $C_\mu = 0.04$ (Fig. 10c), the main jet flow is further widened and vectored away from the synthetic jet. In addition, the main jet is vectored back toward the control side for $x/d_e > 3.5$. When the momentum coefficient is increased further ($C_\mu = 0.08$, Fig. 10d), these trends are much more pronounced, with more of the flow vectored in each direction and the change in vectoring direction occurring farther upstream at $x/d_e \approx 3$. These trends further support the speculation of the two mechanisms associated with the interaction of the synthetic jet with the main jet. Another way to confirm this speculation is to compare the effect of the synthetic jet to that of a steady control jet (see Section 3.3, Fig. 14).

Conversely, when the synthetic jet is activated at $\alpha = 60°$ (Fig. 10e–g for $C_\mu = 0.01$, 0.04, and 0.08, respectively), the main jet spreading is smaller on both sides (compared to the corresponding $\alpha = 30°$ cases). At the low momentum coefficient ($C_\mu = 0.01$, Fig. 10e), the main jet is initially vectored away from the control, and is vectored back for $x/d_e > 3.5$ (unlike the $\alpha = 30°$ case, Fig. 10b). As the momentum coefficient is increased (to $C_\mu = 0.04$ and 0.08, Fig. 10f and g, respectively), the main jet spreading is increased on both sides, but to a lesser extent than the comparable $\alpha = 30°$ cases.

Along the x–z centerline plane for the synthetic jet oriented at both $\alpha = 30°$ and 60° (Fig. 11a–c and d–f, respectively), the velocity vector fields are symmetric about the x-axis and spreading is increased (compared to the baseline). At $C_\mu = 0.01$ (Fig. 11a and d, $\alpha = 30°$ and 60°, respectively), the main jet spreading is similar for both synthetic jet angles. However, as the momentum coefficient is increased to $C_\mu = 0.04$ and 0.08, the synthetic jet oriented at $\alpha = 60°$ (Fig. 11e and f, respectively) increases the main jet's spreading closer to the orifice than the corresponding $\alpha = 30°$ cases (Fig. 11b and c, respectively). This is attributed to the geometric intersection of the synthetic jet centerline and the main jet centerline, which moves farther upstream to $x/d_e = 0.87$ for the $\alpha = 60°$ orientation (compared to 1.5 for the $\alpha = 30°$ case). These results suggest that, by changing the synthetic jet's angle with respect to the main jet centerline to $\alpha = 60°$ from 30°, the synthetic jet's penetration into the main jet is increased (for the same momentum coefficient) while the growth of the naturally unstable modes is reduced, as is discussed in the following paragraph.

To further explore the effect of the orientation of the synthetic jet on the main jet flow field, the phase-averaged flow fields ($\phi = 240°$) of the spanwise and cross-stream vorticity were calculated from the velocity fields and are presented in Figs. 12 and 13,

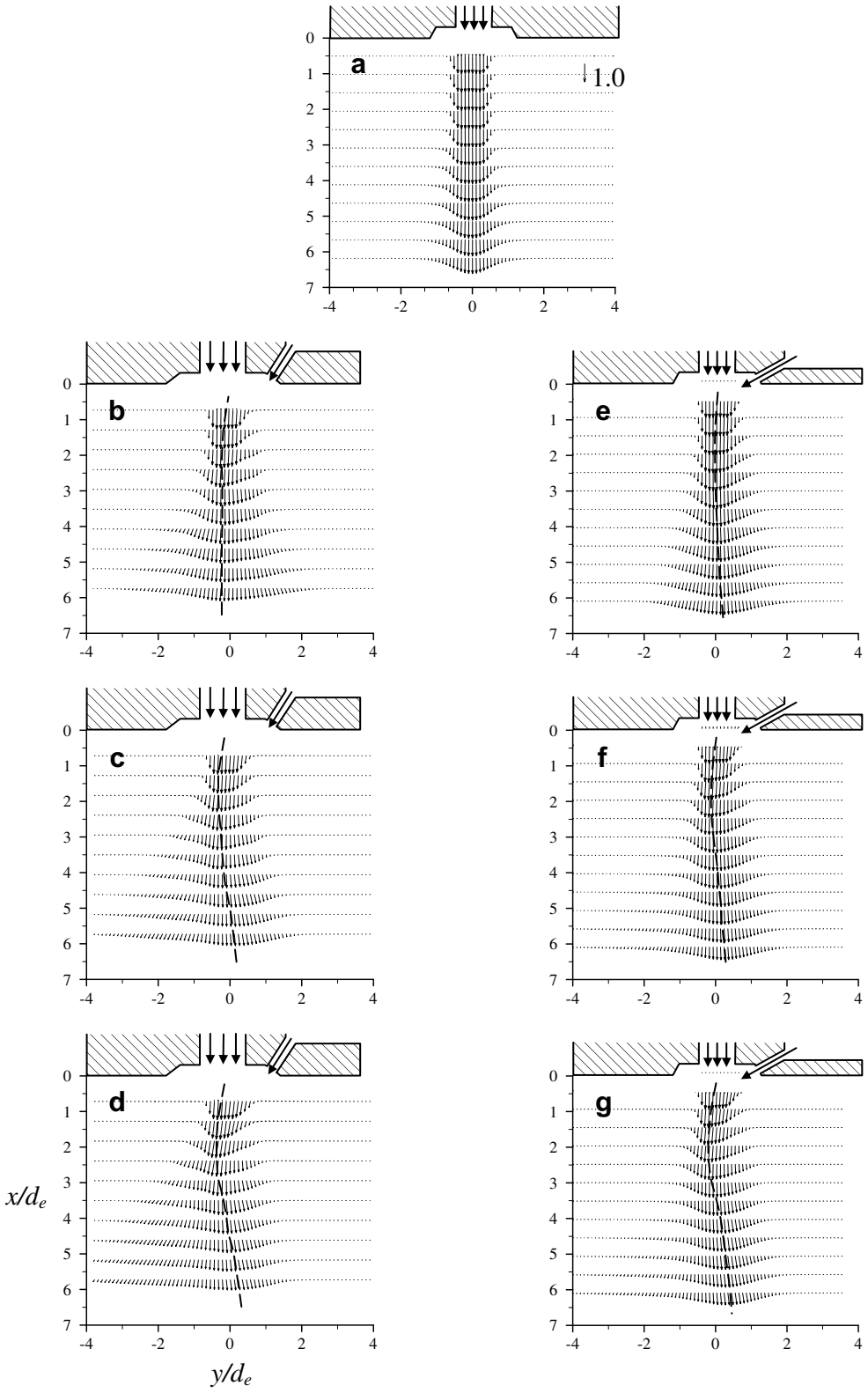

Fig. 10. Velocity vector fields for the baseline (a) and forced jets with $C_\mu = 0.01$ (b, e), 0.04 (c, f), and 0.08 (d, g) with $\alpha = 30°$ (b–d) and 60° (e–g). x–y centerline planes.

respectively. When the synthetic jet is oriented at $\alpha = 30°$ and activated at the lowest momentum coefficient examined ($C_\mu = 0.005$, Fig. 12a), the downstream development of the main jet flow is altered on both sides and large coherent structures are formed. By contrast, when the synthetic jet is oriented at $\alpha = 60°$ (activated at the same C_μ, Fig. 12c), it yields a slight bending of the main jet shape with less spreading than the $\alpha = 30°$ case. Moreover, coherent vortical structures are not formed. At the highest momentum coefficient of $C_\mu = 0.08$ (Fig. 12b and d, $\alpha = 30°$ and 60°, respectively), large coherent structures are formed for both jet angles; however, the extent of the spreading and magnitude of the vortical structures are larger for the synthetic jet at $\alpha = 30°$. Furthermore,

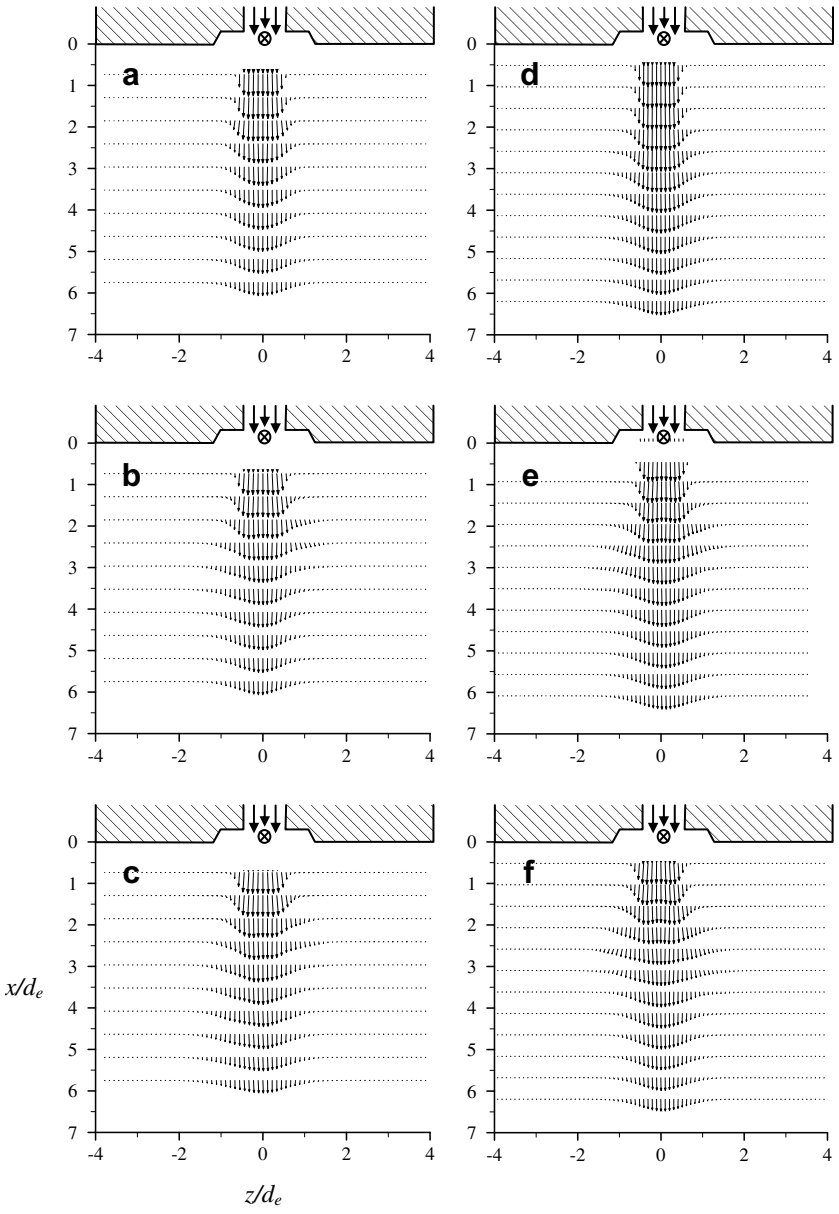

Fig. 11. Velocity vector fields for the forced jets with $C_\mu = 0.01$ (a, d), 0.04 (b, e), and 0.08 (c, f) with $\alpha = 30°$ (a–c) and 60° (d–f). x–z centerline planes.

non-linear interactions are visible (i.e., pairing is observed on the far side of the main jet at $x/d_e = 1.5$ and 4, marked by the bold dash circles).

Fig. 13 presents the vorticity field in the x–z centerline plane. At both momentum coefficients, the synthetic jet oriented at $\alpha = 30°$ produces larger vortical structures and increased spreading compared to the corresponding $\alpha = 60°$ case jet. Note that the arrows (in Fig. 13b and d) mark the impulses from the synthetic jet, which penetrate the x–z centerline plane at $x/d_e \approx 1.8$ and 1.1, for $\alpha = 30°$ and 60°, respectively.

As mentioned above, the effect of the synthetic jet is associated with two mechanisms: (1) direct impact onto the main jet, and (2) amplification of unstable modes of the main jet. The results shown in Figs. 12 and 13 suggest that, by increasing the synthetic jet angle from $\alpha = 30°$ to $\alpha = 60°$ (with the same momentum coefficient), it impacts on the main jet closer to the orifice (where instabilities are very small) disrupts the evolution of the jet, resulting in a smaller growth of the coherent vortical structures. Note, however, that as the angle of the control jet decreases the cross-stream component of the momentum induced by the control jet decreases and, thus, the vectoring of the main jet is reduced. These results are consistent with those presented by Tamburello and Amitay (2007b) where the synthetic jet was oriented perpendicular to the main jet. In that case, activation of the synthetic jet (with the same momentum coefficient, and closest to the main jet exit plane) results, as expected, in larger vectoring of the jet away from the control jet, as well as the largest spreading.

3.3. Comparison between a synthetic jet and a steady control jet

To further understand the contribution of each mechanism, the $\alpha = 60°$ synthetic jet case was compared to the effect of a steady control jet at the same angle such that the effect on the main jet is only due to the penetration (direct impact). The synthetic jet at $\alpha = 60°$ was chosen due to the increased penetration (compared to the $\alpha = 30°$ case). Detailed work on the effect of steady control jets has been previously examined by the authors and is detailed in Tamburello and Amitay (2006, 2007a). In the present work,

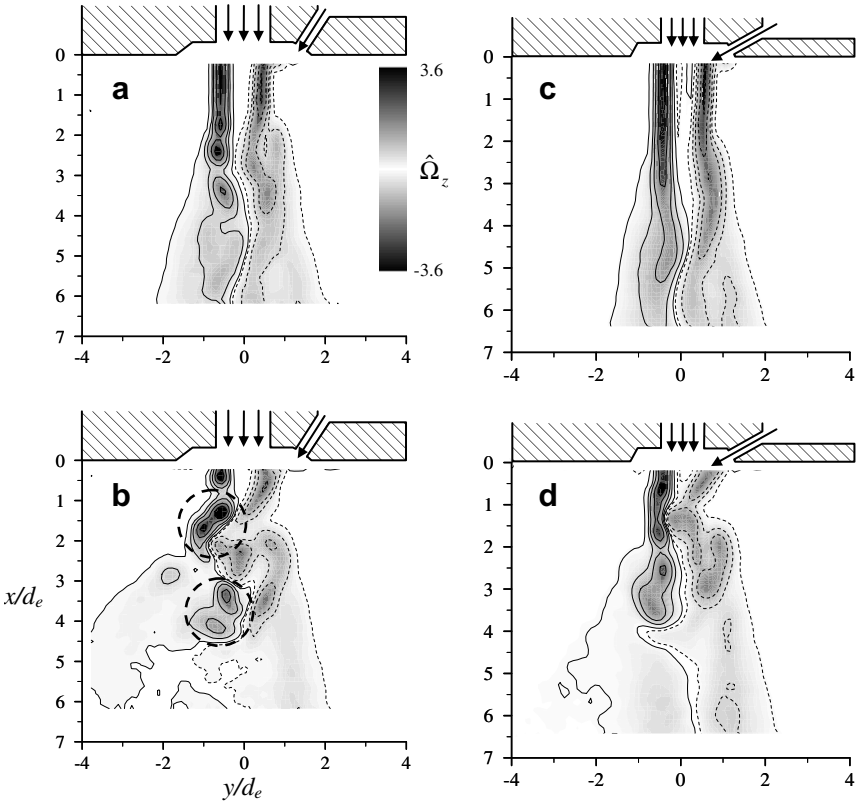

Fig. 12. Phase-averaged spanwise vorticity fields at $\varphi = 240°$ for $C_\mu = 0.005$ (a, c) and 0.08 (b, d) with $\alpha = 30°$ (a–b) and 60° (c–d). x–y centerline plane.

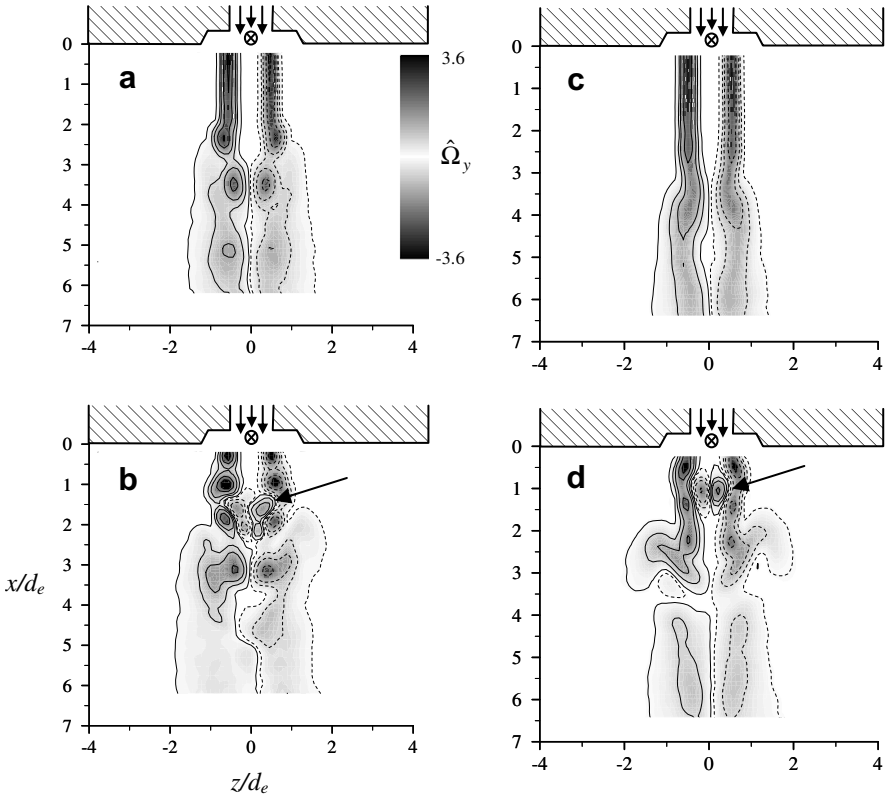

Fig. 13. Phase-averaged cross-stream vorticity fields at $\varphi = 240°$ for $C_\mu = 0.005$ (a, c) and 0.08 (b, d) with $\alpha = 30°$ (a–b) and 60° (c–d). x–z centerline plane.

the focus is on comparing the two control techniques as a tool to examine the effectiveness of the synthetic jet and to decouple the two mechanisms. In the following comparison, both the synthetic jet (SJ) and the steady control jet (CJ) were driven with at

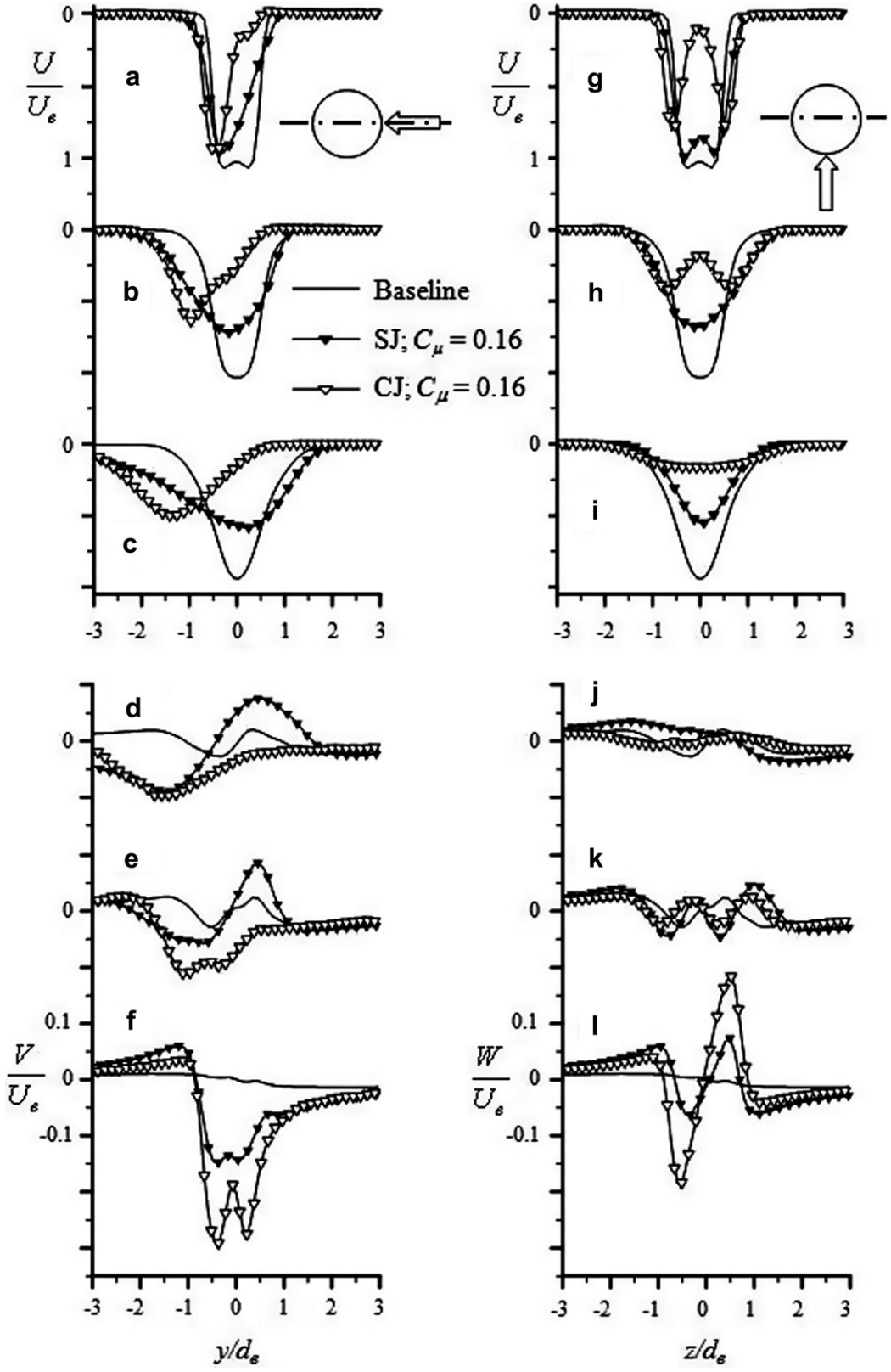

Fig. 14. Streamwise (a–c, g–i), cross-stream (d–f), and spanwise (j–l) velocity profiles at $x/d_e = 1$ (a, f, g, and l), 3 (b, e, h, and k), and 6 (c, d, i, and j).

the highest momentum coefficients tested of 0.16, which showed the greatest contrast in effects. Additional data were taken at lower momentum coefficients and showed similar results, but are not shown for the sake of brevity.

The normalized streamwise (Fig. 14a–c and g–i, x–y and x–z centerline planes, respectively), cross-stream (Fig. 14d–f), and spanwise (Fig. 14j–l) velocity profiles for the baseline and forced jet (steady and synthetic jets) at $x/d_e = 1$ (Fig. 14a, f, g and l), 3

(Fig. 14b, e, h and k), and 6 (Fig. 14c, d, i and j) are presented. Without flow control, the normalized streamwise velocity distributions at $x/d_e = 1$, 3, and 6 are symmetric about the x-axis.

When the synthetic jet is activated, the cross-stream extent of the streamwise velocity component (in the x–y plane) is increased for $x/d_e = 3$ and 6 in both directions (Fig. 14b and c, respectively). However, when the steady control jet is used, it results in lower peak velocities and a vectoring of the main jet away from the control. Since the entire momentum of the steady control jet is used to impact on the main jet, it has a larger effect on the vectoring.

In the x–z centerline plane (Fig. 14g–i), the normalized streamwise velocity profiles have double-peak distributions at $x/d_e = 1$ and are symmetric about the x-axis throughout the flow field for both the control methods. The steady control jet cases also have double-peak distributions at $x/d_e = 3$ as well as wider profiles with lower peak velocities at $x/d_e = 3$ and 6 (Fig. 14h and i, respectively) due to the deeper penetration. When synthetic jet is used, the peak velocity, at all three streamwise locations, is higher than the steady control jet cases.

The baseline velocity profiles of the normalized cross-stream (x–y centerline plane, Fig. 14d–f) and spanwise (x–z centerline plane, Fig. 14j–l) components are anti-symmetric, as expected. When the synthetic jet is activated, there is a significant increase in the cross-stream velocity on both sides of the main jet in the x–y plane at $x/d_e = 1$ and 3 (Fig. 14d and e), which is indicative of increased spreading in both directions. When the steady control jet is used, the cross-stream velocity is negative throughout the measurement plane due to the vectoring away from the control jet.

In the x–z centerline plane (Fig. 14j–l), both the synthetic jet and the steady control jet yield increased spreading (compared to the baseline) of the main jet at all three downstream locations, where the peak magnitudes of the spanwise velocity are larger when continuous control jet is activated.

Fig. 14 shows that a steady control jet, which utilize only the direct impact mechanism, results in vectoring and a deep penetra-

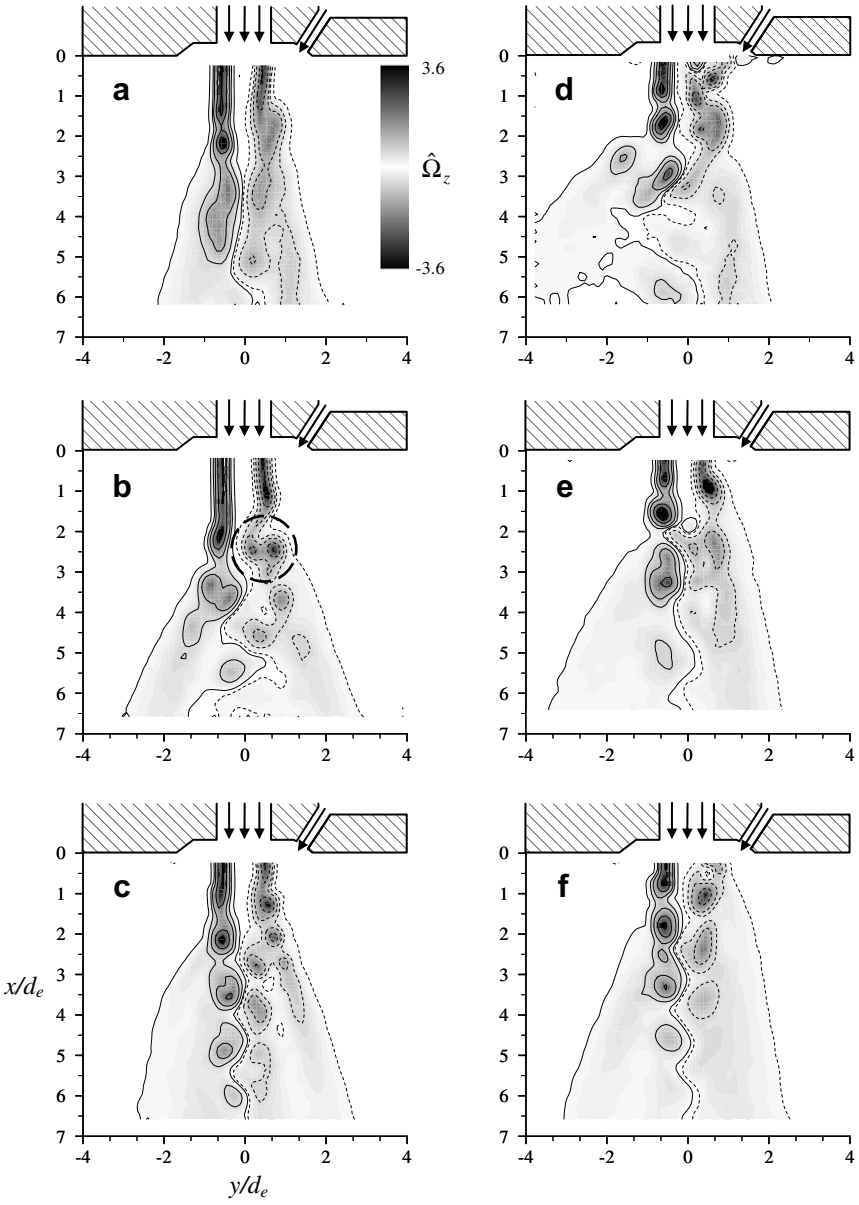

Fig. 15. Phase-averaged spanwise vorticity fields at $\phi = 240°$ for $C_\mu = 0.005$ (a–c) and 0.08 (d–f) with $St_r = 0.16$ (a, d), 0.32 (b, e), and 0.48 (c, f). x–y centerline plane.

tion into the main jet. However, when the synthetic jet is activated, having both the direct impact onto the main jet as well as the amplification of its unstable modes, the main jet exhibits increased spreading both toward and away from the control jet.

3.4. Effect of the synthetic jet's actuation frequency

Next, the effect of the Strouhal number on the amplification of the main jet natural modes and the interaction mechanisms were quantified, where the synthetic jet actuation frequency was increased from 1000 Hz to 2000 Hz and 3000 Hz (St_r = 0.16, 0.32, and 0.48, respectively). Fig. 15 presents the phase-averaged (ϕ = 240°) vorticity distributions for the St_r = 0.16 (Fig. 15a and d), 0.32 (Fig. 15b and e), and 0.48 (Fig. 15c and f) with α = 30° and C_μ = 0.005 (Fig. 15a–c) and 0.08 (Fig. 15d–f) along the x–y centerline plane. When the synthetic jet is activated at C_μ = 0.005, large vortical structures are formed that are more distinct and coherent with increasing Strouhal number. Note that the streamwise wavelength of these structures decreases with increasing Strouhal number, as expected. Also, for the moderate Strouhal number (St_r = 0.32, Fig. 15b) pairing of the vortical structures, as marked by the dashed circle, is clearly visible. At this Strouhal number, the synthetic jet creates the largest main jet spreading (compared to the other two Strouhal numbers at C_μ = 0.005) due to the largest growth rate associated with this non-dimensional frequency (inviscid linear stability analysis, Criminale et al., 2003).

At C_μ = 0.08 (Fig. 15d–f), each of the vorticity distributions contains distinct, coherent structures near the main jet exit that merge together and lose their coherence farther downstream. In addition, the main jet is vectored farthest from the control jet for St_r = 0.16 (Fig. 15d), and the vectoring decreases with increasing Strouhal number. As was mentioned above, synthetic jet flow control incorporates two mechanisms, impulse and amplification. For the low Strouhal number controlled jet, the amplification rate is the smallest and, therefore, its penetration is larger than for the other two. Moreover, at this high C_μ it is very likely that the excited modes saturate.

In the x–z centerline plane, the St_r = 0.48 case at C_μ = 0.005 (Fig. 16a) has the most distinct, coherent structures. At C_μ = 0.08, for all three cases, the structures lose coherence by $x/d_e \approx 3$ due to the vectoring of the jet off of the measurement plane.

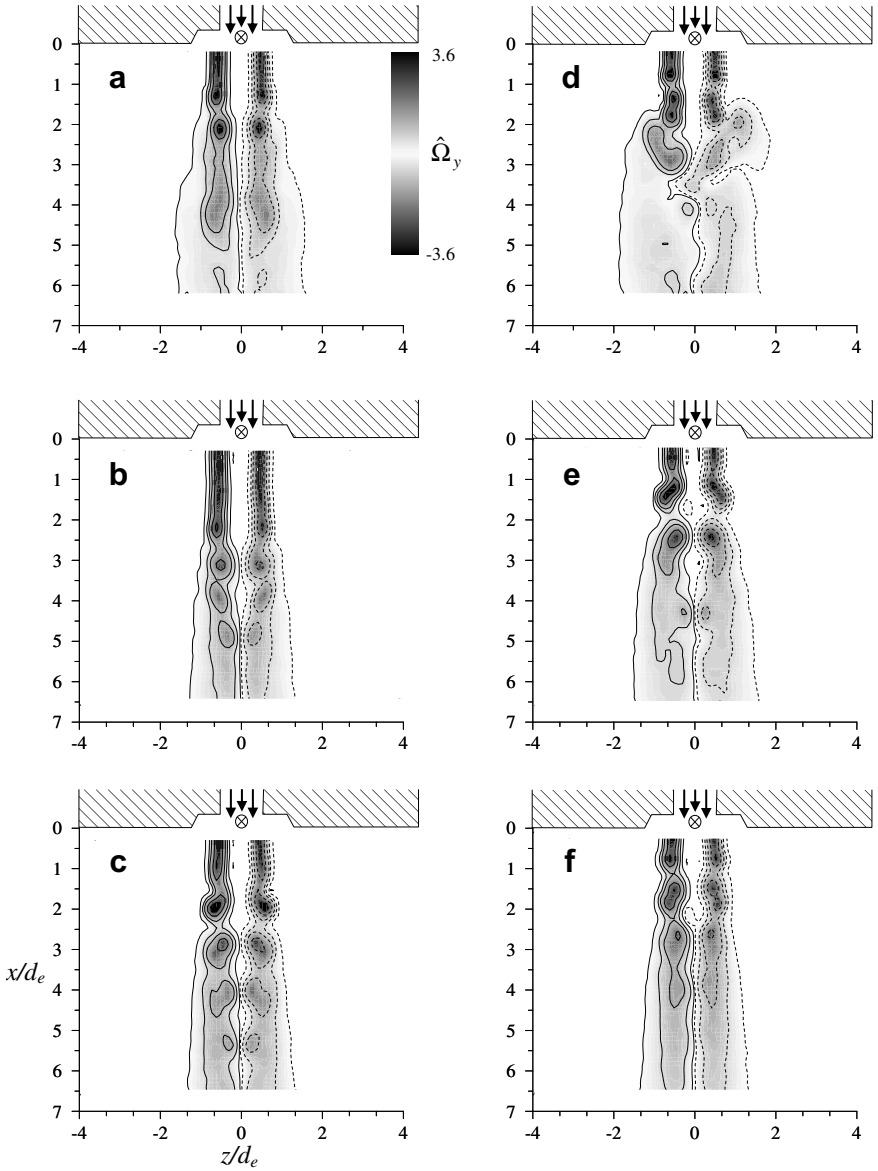

Fig. 16. Phase-averaged cross-stream vorticity fields at ϕ = 240° for C_μ = 0.005 (a–c) and 0.08 (d–f) with St_r = 0.16 (a, d), 0.32 (b, e), and 0.48 (c, f). x–z centerline plane.

According to Crow and Champagne (1971), the preferred mode of an axisymmetric, transitional free jet corresponds to a Strouhal number of 0.3. While other authors have found different values (e.g., $St_r = 0.6$, Beavers and Wilson, 1970; $St_r = 0.24$–0.51, Gutmark and Ho, 1983; $St_r = 0.3$, Kaster et al., 2004; and others), these differences have been attributed to variations in the boundary conditions at the nozzle exit (Cohen and Wygnanski, 1987) as well as the uncertainty in the measurements (Petersen and Samet, 1988). Thus, the $St_r = 0.32$ case at $C_\mu = 0.005$ (x–y centerline, Fig. 15b) corresponds to the preferred modes, as is shown in the distinct structures and increased jet width (compared to $St_r = 0.16$ and 0.48). However, as the momentum coefficient is increased, the $St_r = 0.32$ case no longer has the largest effect on the main jet, as shown for $C_\mu = 0.08$ (Fig. 15d–f).

One possible explanation for this disparity is the amplitude of the synthetic jet excitation. Linear stability analysis assumes a *small* perturbation, which may be assumed for the lowest momentum coefficient ($C_\mu = 0.005$). However, at the higher momentum coefficients, the maximum peak velocity during the blowing portion of the synthetic jet actuation cycle becomes larger than the main jet exit velocity (e.g., 72 m/s for $C_\mu = 0.16$ with $U_e = 25$ m/s) and the main jet flow field is highly distorted (e.g., iso-velocity surfaces in Fig. 4). Thus, at these higher momentum coefficients, the linear stability and weakly non-linear stability analysis are no longer applicable. Nallasamy and Hussain (1983) showed that, for a fixed Strouhal number, the turbulent fluctuations saturate with increasing excitation amplitude. In addition, they showed that the instability growth rate decreased with increasing excitation amplitude for high-amplitude excitations.

4. Conclusions

This paper examines, experimentally, the manipulation of an axisymmetric, transitional jet ($\mathrm{Re}_{U_e} = 6600$) using a single synthetic jet that is mounted at either 30° or 60° angles with respect to the main jet centerline. This work provides an in depth investigation of the complex three-dimensional interaction between the synthetic jet and the main jet flow by utilizing a three-dimensional rendering technique based on multiple two-dimensional measurement planes. The synthetic jet was driven at frequencies of 1000 Hz, 2000 Hz, and 3000 Hz ($St_r = 0.16$, 0.32, and 0.48, respectively), which correspond to the natural unstable modes in the main jet's flow field and, thus, take advantage of naturally amplifying structures within the main jet flow. The present research provides additional insight into controlling the turbulence level, spreading, and direction of a transitional, axisymmetric jet using active flow control for various control parameters.

When the synthetic jet is activated at a 30° angle, with $St_r = 0.16$, it penetrates into the main jet, bends its vortical structures, and tilts them in the streamwise direction, resulting in counter-rotating streamwise vortices that wrap around the synthetic jet's impulse. As the synthetic jet momentum coefficient is increased, it penetrates deeper into the main jet and its presence is much more pronounced in both the magnitude of its streamwise vortical structures as well as in the main jet's pair of streamwise counter-rotating rollers that wrap around the synthetic jet's impulse.

In addition, the synthetic jet significantly increased the main jet's turbulence quantities, especially near the interaction domain. Using triple decomposition, it was shown that near the interaction region the random and coherent motions have similar contributions to the turbulent stresses; whereas the coherent motions prevail farther downstream (and along the shear layers).

There are two mechanisms involved in the interaction between a synthetic jet and the main jet: (1) the direct impact of the synthetic jet into the main jet, and (2) the amplification of the main jet's naturally unstable modes. By changing the synthetic jet's angle from 30° to 60°, the effect of the synthetic jet is somewhat decreased. This might be attributed to the location of the interaction that moved farther upstream into the potential core.

Utilizing only the direct impact mechanism, a steady control jet also results in vectoring away from the control jet and a deep penetration into the main jet. However, without the amplification of its unstable modes, the main jet exhibits decreased spreading compared to a synthetic jet with the same momentum coefficient.

The effect of the synthetic jet's frequency was also examined and can be divided into two regimes: low C_μ, where the largest effect is obtained for $St_r = 0.32$, and high C_μ, where the excitation level is very high such that saturation is obtained.

In conclusion, a single synthetic jet can significantly alter the development of an axisymmetric free jet. By changing the synthetic jet's momentum coefficient, its angle with respect to the main jet centerline, and its driving frequency, the relative contribution of each mechanism to the synthetic jet's effects on the main jet flow field can be controlled.

Acknowledgement

This work has been supported by RPI's internal funding.

References

Ahuja, K.K., 1993. Mixing enhancement and jet noise reduction through tabs plus ejectors. AIAA Paper 93-4347.
Ahuja, K.K., Lepicovsky, J., Burrin, R.H., 1982. Noise and flow structure of a tone-excited jet. AIAA Journal 20, 1700–1706.
Alkislar, M.B., Choutapalli, I., Krothapalli, A., Lourenco, L.M., Arakeri, J.H., 2005. The structure of a pulsed jet – a PIV study. AIAA Paper 2005-1274.
Alvi, F.S., Krothapalli, A., Washington, D., King, C.J., 2000. Active control of supersonic impinging jets using microjets. AIAA Paper 2000-2236.
Amitay, M., Cannelle, F., 2006. Evolution of finite span synthetic jets. Physics of Fluids 18 (054101), 1–16.
Arakeri, V.H., Krothapalli, A., Siddavaram, V., Alkislar, M.B., Lourenco, L.M., 2003. On the use of microjets to suppress turbulence in a Mach 0.9 axisymmetric jet. Journal of Fluid Mechanics 490, 75–98.
Beavers, G.S., Wilson, T.A., 1970. Vortex growth in jets. Journal of Fluid Mechanics 44 (1), 97–112.
Bradbury, L.J.S., Khadem, A.H., 1975. The distortion of a jet by tabs. Journal of Fluid Mechanics 70, 801–813.
Cannelle, F., Amitay, M., 2005. Synthetic jets: spatial evolution and transitory behavior. AIAA Paper 2005-0102.
Cohen, J., Wygnanski, I., 1987. The evolution of instabilities in the axisymmetric jet. Part 1. The linear growth of disturbances near the nozzle. Journal of Fluid Mechanics 176, 191–219.
Criminale, W.O., Jackson, T.L., Joslin, R.D., 2003. Theory and Computation of Hydrodynamic Stability. Cambridge University Press, New York, NY.
Crow, S., Champagne, F.M., 1971. Orderly structures in jet turbulence. Journal of Fluid Mechanics 48, 547–591.
Davis, S.A., 2000. The manipulation of large- and small-scale flow structures in single and coaxial jets using synthetic jet actuators. Doctoral Thesis, Georgia Institute of Technology.
Davis, S.A., Glezer, A., 2000. The manipulation of large- and small-scales in coaxial jets using synthetic jet actuators. AIAA Paper 2000-0403.
Glezer, A., Amitay, M., 2002. Synthetic jets. Annual Review of Fluid Mechanics 34, 503–529.
Gutmark, E.J., Grinstein, F.F., 1999. Flow control with noncircular jets. Annual Review of Fluid Mechanics 31, 239–272.
Gutmark, E.J., Ho, C., 1983. On the preferred modes and the spreading rates of jets. Physics of Fluids 26, 2932–2938.
Hileman, J., Caraballo, E., Samimy, M., 2003. Simultaneous real-time flow visualizations and acoustic measurements on a tabbed Mach 1.3 jet. AIAA Paper 2003-3123.
Ho, C., Gutmark, E.J., 1987. Vortex induction and mass entrainment in small-aspect-ratio elliptical jet. Journal of Fluid Mechanics 179, 383–405.
Ibrahim, M.K., Kunimura, R., Nakamura, Y., 2002. Mixing enhancement of compressible jets by using unsteady microjets and actuators. AIAA Journal 40 (4), 681–688.
Kaster, J., Hileman, J., Samimy, M., 2004. Exploring high-speed axisymmetric jet noise control using Hartmann tube fluidic actuators. AIAA Paper 2004-0186.
Nallasamy, M., Hussain, A.K.M.F., 1983. Numerical study of the phenomenon of turbulence suppression in a plane shear layer. Turbulent Shear Flows 4, 169–181.

New, T.H., Tay, W.L., 2004a. Effects of circumferential microjets on the near-field behavior of a round jet. AIAA Paper 2004-0923.
New, T.H., Tay, W.L., 2004b. Cross-stream radial fluid injection into a round jet. AIAA Paper 2004-2403.
Pack, L.G., Seifert, A., 2001. Periodic excitation for jet vectoring and enhanced spreading. Journal of Aircraft 38 (3), 486–495.
Petersen, R.A., Samet, M.M., 1988. On the preferred mode of jet instability. Journal of Fluid Mechanics 194, 153–173.
Pothos, S., Longmire, E.K., 2001. Asymmetric forcing of a turbulent rectangular jet with a piezoelectric actuator. Physics of Fluids 13 (5), 1480–1491.
Reeder, M.F., Samimy, M., 1996. The evolution of a jet with vortex-generating tabs: real-time visualization and quantitative measurements. Journal of Fluid Mechanics 311, 73–118.
Sakakibara, K., Hishida, K., Phillips, W.R.C., 2001. On the vortical structure in a plane impinging jet. Journal of Fluid Mechanics 434, 273–300.
Schabacker, J., Bölcs, A., 1996. Investigation of turbulent flow by means of the PIV method. In: 13th Symposium on Measuring Techniques for Transonic and Supersonic Flows in Cascades and Turbomachines, Zurich, Switzerland, September 5–6, 1996.
Seidel, J.-F., Pappert, C., New, T.H., Tsai, H.M., 2005. Effects of multiple radial blowing around a circular jet. AIAA Paper 2005-866.
Smith, B.L., Glezer, A., 1998. The formation and evolution of synthetic jets. Physics of Fluids 10 (9), 2281–2297.
Smith, B.L., Glezer, A., 2002. Jet vectoring using synthetic jets. Journal of Fluid Mechanics 458, 1–34.
Tamburello, D., Amitay, M., 2006. Manipulation of an axisymmetric jet using continuous control jets. Journal of Turbulence 7 (59), 1–24.
Tamburello, D., Amitay, M., 2007a. Interaction of a free jet with a perpendicular control jet. Journal of Turbulence 8 (21), 1–27.
Tamburello, D., Amitay, M., 2007b. Three-dimensional interactions of a free jet with a perpendicular synthetic jet. Journal of Turbulence 8 (38), 1–21.
Tamburello, D., Amitay, M., 2007c. Dynamic response of a free jet to the activation of a single synthetic jet. Journal of Turbulence 8 (48), 1–18.
Wicker, R.B., Eaton, J.K., 1994. Near field of a coaxial jet with and without axial excitation. AIAA Journal 32 (3), 542–546.
Wiltse, J.M., Glezer, A., 1993. Manipulation of free shear flows using piezoelectric actuators. Journal of Fluid Mechanics 249, 261–285.
Wiltse, J.M., Glezer, A., 1998. Direct excitation of small-scale motions in free shear flows. Physics of Fluids 10 (8), 2026–2036.
Yule, A.J., 1978. Large-scale structure in the mixing layer of a round jet. Journal of Fluid Mechanics 89, 413–432.
Zaman, K.B.M.Q., 1999. Spreading characteristics of compressible jets from nozzles of various geometries. Journal of Fluid Mechanics 383, 197–228.
Zaman, K.B.M.Q., Reeder, M.F., Samimy, M., 1994. Control of an axisymmetric jet using vortex generators. Physics of Fluids 6 (2), 778–793.